JOURNAL OF APPLIED CRYSTALLOGRAPHY

ISSN 1600-5767

A JUNGFRAU-based electron diffractometer with large-scale capacity

Kiyofumi Takaba,[a,b]* Khalil Ferjaoui,[b] Erik Fröjdh[b] and Tim Gruene[a]

[a]Institute of Inorganic Chemistry, University of Vienna, Vienna, Austria, and [b]Paul-Scherrer-Institut, Villigen, Switzerland. *Correspondence e-mail: kiyofumi.takaba@psi.ch

Received 27 June 2026
Accepted 8 September 2026

Edited by S. Boutet, SLAC National Accelerator Laboratory, Menlo Park, USA

Keywords: three-dimensional electron diffraction; JUNGFRAU detector; charge-density analysis; adaptively conditioned measurement.

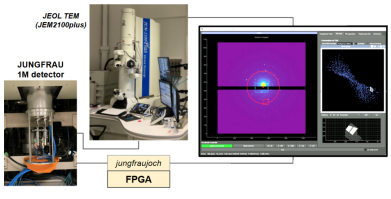
CCDC references: 2535387; 2535389; 2586536; 2586537; 2586538; 2586539; 2586540

Supporting information: this article has supporting information at journals.iucr.org/j

An integrated hardware–software platform for three-dimensional electron diffraction has been developed using the JUNGFRAU 1M charge-integrating hybrid pixel detector. The system combines the field-programmable gate array based Jungfraujoch backend with the *JFGui* graphical interface, providing centralized control of the detector, electron microscope and data-processing software. This workflow enables synchronized data acquisition, live visualization and instantaneous post-processing with established crystallographic programs, including *XDS*, *DIALS* and *SHELX*. Applications to L-histidine and dioctyl perylene tetracarboxylic diimide crystals are presented, including charge-density evaluation employing the recently developed iSFAC (ionic scattering factors) model. The workflow supports continuous-rotation measurements at speeds up to 10° s^{-1}, allowing acquisition of a ∼130° rotation in approximately 15 s and enabling higher-throughput measurements. Comparative measurement at 100 and 200 keV beam energies revealed the trade-off between real-space contrast and diffraction resolution. These developments establish a complete and efficient practical workflow of 3D ED coupled with instrumental evaluation, providing a robust route toward quantitative electron crystallography.

1. Introduction

Structure determination using three-dimensional electron diffraction (3D ED) has emerged as a powerful technique over the past 15 years. Owing to its applicability to sub-micrometre-sized crystals, it has enabled the elucidation of structures across diverse fields of chemistry. Continuous developments in methodology and instrumentation have further expanded its capabilities, resulting in several variants of 3D ED techniques (Smeets *et al.*, 2018; Gemmi *et al.*, 2019; Yörük *et al.*, 2024). Another notable advantage of 3D ED lies in the higher sensitivity of electron scattering to charge density compared with X-ray diffraction (Zuo *et al.*, 1999; Yonekura *et al.*, 2018; Takaba *et al.*, 2023). Pioneering studies have demonstrated its potential for experimental evaluation of charge distribution within molecules, highlighting a unique strength of electron-based approaches (Suresh *et al.*, 2024; Pacoste *et al.*, 2024; Mahmoudi *et al.*, 2025). Despite these advantages, 3D ED has not yet become a mainstream method for structure determination. The Cambridge Structural Database [Cambridge Crystallographic Data Center (CCDC)] (Groom *et al.* (2016) lists 239 entries in the electron diffraction subset for the period 2022–2024, corresponding to 0.140% of all new entries. Even when accounting for limited instrument availability, this indicates that 3D ED remains far from being a first-choice technique, despite the less stringent requirements for crystal growth compared with X-ray diffraction. Currently, 3D ED and its advanced applications still require more time and



OPEN ACCESS
Published under a CC BY 4.0 licence

effort than conventional methods. Unless these limitations are addressed, the broader impact of 3D ED and the structural insights that can be provided to chemistry, *e.g.* drug design, materials science and charge-density analysis, will remain constrained.

In 3D ED, a diffraction volume can be collected from a single crystal on a transmission electron microscope (TEM) grid with continuous stage rotation. However, in application to organic chemistry, limited lattice symmetry, variations in crystallinity and heterogeneity in crystal grain morphologies often necessitate collection of multiple datasets and their merging. Several software packages have been developed to enable sequential data collection, including *SerialEM* (Mastronarde, 2005; de la Cruz *et al.*, 2019; Takaba *et al.*, 2020; Sasaki *et al.*, 2023), *Instamatic* (Wang *et al.*, 2019; Roslova *et al.*, 2020), *EPU-D* (Thermo Fisher Scientific) and *CrysAlis*^{Pro} for ED (Rigaku) (Ito *et al.*, 2021). Considering the instability of the electron beam on events inducing fluctuations, it is appropriate to collect diffraction datasets from multiple crystals maintaining the beam condition unchanged. This is particularly true for active-pixel sensor detectors, where changes in beam conditions risk detector damage from unexpected direct-beam incidence. Consequently, a uniform exposure rate is usually adopted. In addition, to account for the lower dose tolerance of crystals of smaller volume sampled across a collection sequence, a reduced exposure rate tends to be preferred. An exposure of $\sim$1 e$^-$ Å^{-2} per single rotation is often selected, following the applications for macromolecules, which are the most beam-sensitive targets of 3D ED (Gruene *et al.*, 2018; Ito *et al.*, 2021; Martynowycz *et al.*, 2022). Although this strategy is reasonable for samples containing limited types of elements and structural motifs, the optimal irradiation conditions should depend on sample composition and the target precision: heavier elements and aromatic systems may tolerate higher doses (Egerton, 2019), whereas higher-precision studies require reduced exposure (Howells *et al.*, 2009).

Hybrid pixel detectors allow beam conditions to be changed without special consideration for TEM operation thanks to their radiation hardness, with which even direct-beam irradiation is feasible. The JUNGFRAU is a charge-integrating hybrid pixel detector initially developed for X-ray free-electron lasers (XFELs) and synchrotron applications (Mozzanica *et al.*, 2016; Leonarski *et al.*, 2018). Similarly to other hybrid pixel detectors, such as Timepix (Genderen *et al.*, 2016), EIGER (Tinti *et al.*, 2018) and SINGLA (Parkhurst *et al.*, 2023), its application to electron diffraction has been proposed (Fröjdh *et al.*, 2020). Compared with these counting detectors, JUNGFRAU offers a linear response over a wider dynamic range (Leonarski *et al.*, 2018; Fröjdh *et al.*, 2024). The in-pixel gain switching provides a dynamic range of 120 MeV px^{-1} frame^{-1} with 2 kHz frame rate, which corresponds to 1.2×10^6 e$^-$ px^{-1} s^{-1} for 200 kV electrons. Accurate measurement of both intense and weak diffraction spots is particularly important when aiming to quantify charge distribution in crystals, since photons and electrons scatter differently from core and valence charge over a broad scattering angle range.

To harness these advantages for practical 3D ED, an integrated hardware–software system is essential for end-users to conduct data collection efficiently. A field-programmable gate array (FPGA)-based backend, Jungfraujoch, has been developed as a control and readout system for data acquisition at synchrotron beamlines with JUNGFRAU, operating at 2 kHz (Leonarski *et al.*, 2023). Building on this, we developed an integrated framework that couples JUNGFRAU and Jungfraujoch to a JEOL electron microscope via a user interface, *JFGui* (Ferjaoui *et al.*, 2025). Following the initial demonstration of the detector platform, successive developments have transformed *JFGui* into an integrated environment for routine 3D ED measurements. In addition to the synchronization between data acquisition and crystal rotation, the current implementation incorporates live visualization, calibration in both real and reciprocal space, and integrated post-processing, allowing users to perform all essential experimental operations within a single interface. Thus, insights into sample properties can be obtained at the earliest measurement stages, allowing beam conditions to be adaptively tuned. The system is designed with extensibility in mind, between the JUNGFRAU and the modern electron microscopy setups.

In the following sections we introduce the *EPOC* (*Electrostatic Potential of Compounds*) software suite, focusing on its function for 3D ED. We then demonstrate its capabilities on cases for organic samples. Applications of the simplest charge-density analysis, iSFAC (ionic scattering factors), which we recently proposed (Mahmoudi *et al.*, 2025), are presented as an aim of the workflow. Exploiting the features of JUNGFRAU aligned with the developed software, the feasibility and efficiency of high-speed rotation measurement and lower-energy beams are verified to elucidate the performance and limitations of the current instrument.

2. Materials and methods

2.1. Sample preparation

Crystals of L-histidine (Fluka) were taken directly from the bottle and suspended in *n*-hexane. The suspension was sonicated to crush and disperse the crystalline grains. Dioctyl perylene tetracarboxylic diimide (PTCDI-C8) nanowires were prepared following the reported procedure (Briseno *et al.*, 2007); thin red crystals were precipitated from methanol. Perylene powder (FUJIFILM Wako) was dissolved in acetone, and the solution was injected into vigorously stirred water using a Hamilton syringe injector, resulting in the immediate formation of crystalline grains (Li *et al.*, 2019). For all samples, a few microlitres of the suspension were dropped onto a copper grid coated with a lacey-carbon film and air-dried for several minutes. Each grid was inserted into the column of the electron microscope using a single-tilt cryo-sample holder, Gatan Elsa Model 698 (GATAN). The operating room temperature was maintained at 22°C, and the sample temperature control of the holder was used only for cryo-measurements.

2.2. Hardware and software framework

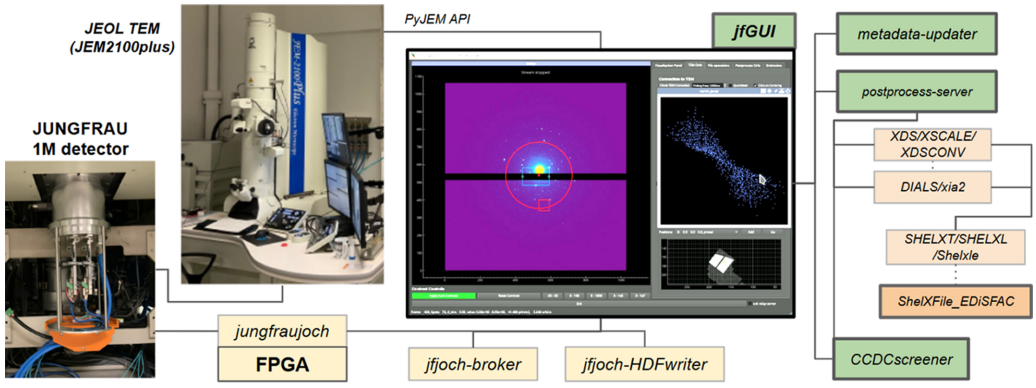
2.2.1. System overview

The hardware architecture and the basic workflow for single-rotation collection have been described previously (Ferjaoui *et al.*, 2025). In summary, the JUNGFRAU 1M detector was mounted on a JEOL JEM2100Plus transmission electron microscope. The projected images on the detector are acquired through a Linux server running the FPGA-accelerated framework Jungfraujoch (Leonarski *et al.*, 2023). Jungfraujoch manages measurement control (start/stop/cancel) through the *jfjoch_broker* and saves images via the *jfjoch_writer*. The microscope is operated using its console and *PyJEM*, the Python-based interface, version 3.8 (JEOL, 2018). All components communicate through *JFGui*, a Qt-based graphical user interface developed for this setup and derived from *SinglaGUI* (Maisriml & Gruene, 2024). *JFGui* runs on a dedicated Linux workstation to avoid resource contention during image acquisition. It communicates with the microscope PC via a relay script, *simple-tem*, which wraps the *PyJEM* API and exposes a small command interface used by *JFGui* to send control commands and receive real-time status updates from the TEM.

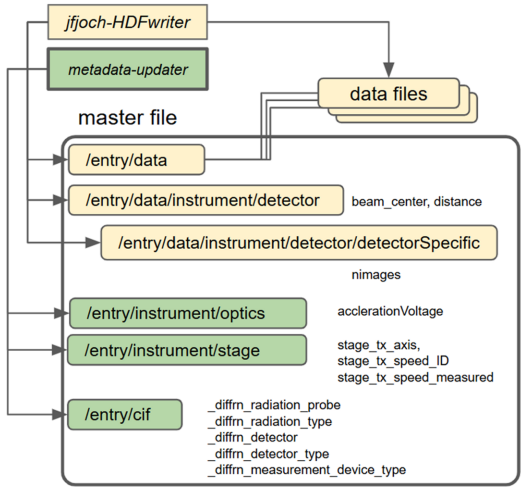
Communication between Jungfraujoch and *JFGui* is managed by a wrapper from *epoc-utils*, ensuring synchronization between user control and acquisition servers. Status values (*e.g.* lens conditions, stage position, camera settings) are saved as metadata within an HDF5 master file alongside image frames. A Python utility, *metadata-updater*, handles this information for later use during post-processing by the *PostprocessServer_JFED*. A separate *CCDCscreener* script queries crystal information from the CCDC. *ShelXFile_EDiSFAC*, an extension of the *SHELXL* (Sheldrick, 2015*a*) parser *ShelXFile* (Kratzert, 2018), allows quick application of the iSFAC modeling and its visualization for evaluation of atomic charge distributions (Mahmoudi *et al.*, 2025). Fig. 1 illustrates the interconnections between these software components and the structure of the resulting HDF5 output.

2.2.2. Live visualization

JFGui receives the live image stream from Jungfraujoch, processed on the FPGA where frame summation is performed



(*a*)



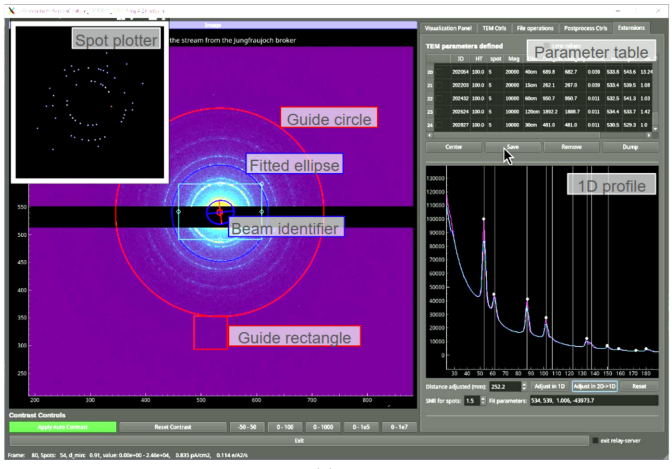
(*b*)

Figure 1
Hardware and software configuration. (*a*) Central role of *JFGui* in coordinating communication between hardware and software components. (*b*) Representative metadata structure stored within the HDF5 output file; only major tags are shown.

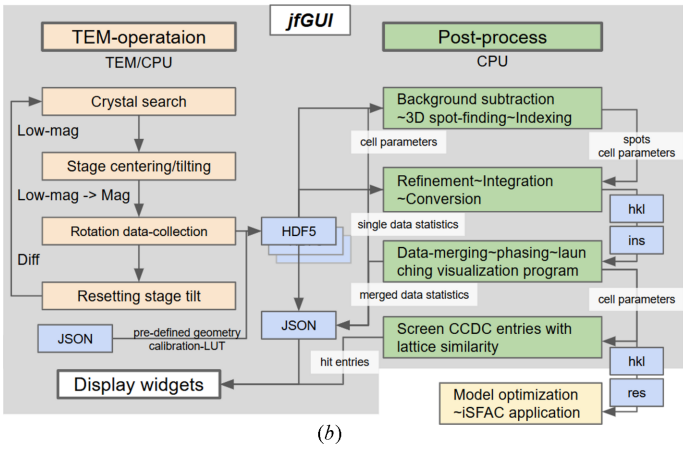
before transmission. Users can toggle between automatic and preset contrast settings to visualize both real-space and diffraction images. In LowMAG mode, images are down-sampled and arranged into a grid atlas. Beam intensity is estimated from the modal pixel value corresponding to the open-grid area. *JFGui* reports electron dose as intensity scaled by the illuminated area, expressed in $Å^{-2}\ s^{-1}$. In DIFF mode, the software quantifies beam shape from peak height and width, identifies the beam center, and uses this for FPGA-based spot finding. Detected spot properties are sent back to *JFGui* to estimate diffraction resolution. These spots are also referenced to assess elliptical distortion in the calibration mode (see Section 2.2.3). Combining spot coordinates with the stage tilt allows visualization of the diffraction pattern in 3D reciprocal space. These visualization features operate at $\geq$20 frames per second, enabling fully interactive, real-time feedback during data collection.

2.2.3. Calibration

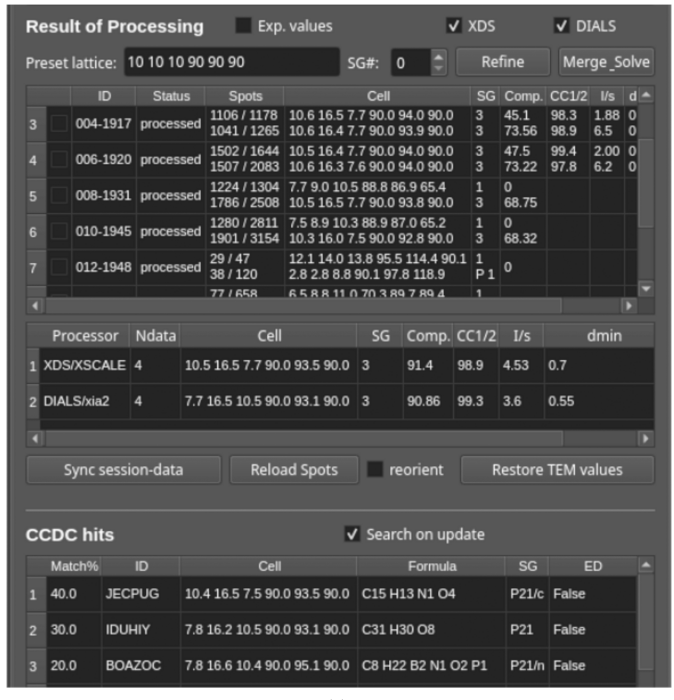
Magnification calibration in both real and reciprocal space is handled through lookup tables (LUTs) that map nominal to measured values. Real-space magnification is determined using a grating grid (TED PELLA). In reciprocal space, the magnification can be termed camera length, which depends not only on the nominal value but also on other parameters constructing the beam path, such as the operating accelerating voltage, probe size and any other conditions that can vary due to the hysteresis of electromagnetic lenses. The current implementation interpolates the determined values sampled across three major parameters: accelerating voltage, magnification and nominal camera length. The LUT is constructed from Debye–Scherrer ring measurements of an evaporated aluminium standard grid (Agar Scientific) under various configurations. Standard distances are obtained by azimuthal



(*a*)



(*b*)



(*c*)

Figure 2
JFGui features and data-processing workflow. (*a*) Calibration measurement interface showing beam and magnification evaluation; labels with gray background are external annotations. A guide rectangle is used for centering between LowMAG and MAG modes. (*b*) Flow chart summarizing the data-collection and processing workflow; gray-shaded steps are directly controllable through the GUI. (*c*) Representative display of multiple datasets collected and merged. Results from *XDS* and *DIALS* appear in paired rows of the top table. After several datasets have been collected, data-merging can start, and the output is shown in the middle table. If CCDC depositions with similar lattice parameters to the determined ones are identified, they are listed in the bottom table. The matches in the *ELECTRON* subset are checked.

Table 1
Measurement parameters and data collection statistics for L-histidine.

		L-Histidine			
Molecular formula		$C_6H_9N_3O_2$	$C_6H_9N_3O_2$	$C_6H_9N_3O_2$	$C_6H_9N_3O_2$
Sample temperature (K)		295	295	163	163
Detector		JUNGFRAU 1M	JUNGFRAU 1M	JUNGFRAU 1M	JUNGFRAU 1M
Frame rate (Hz)		2000	2000	2000	2000
Frames summed		100	20	100	20
Data collection					
Electron microscope		JEOL JEM2100Plus	JEOL JEM2100Plus	JEOL JEM2100Plus	JEOL JEM2100Plus
Accelerating voltage (kV)		200	200	200	200
Electron count rate ($Å^{-2}\,s^{-1}$)		0.02	0.11	0.02	0.11
Duration per single data collection (s)†		50.7–70.2	12.8–16.5	51.6–60.5	11.7–15.5
Rotation angle range (°)†		101.9–140.5	108.2–138.2	103.7–120.6	99.7–128.9
Stage rotation speed ($^\circ\,s^{-1}$)	Nominal	2.0	10.0	2.0	10.0
	Measured†	2.016 (3)	8.9 (2)	2.018 (1)	8.9 (1)
Camera length (mm)	Nominal	500	500	500	500
	Calibrated	750	750	750	750
Crystallographic data					
Processing software		*DIALS*	*DIALS*	*DIALS*	*DIALS*
Merging software		*xia2*	*xia2*	*xia2*	*xia2*
Number of crystal merged		8	9	5	11
Space group		$P2_12_12_1$	$P2_12_12_1$	$P2_12_12_1$	$P2_12_12_1$
a, b, c (Å)		5.2079(8), 7.4211 (16), 19.021 (4)	5.2690 (13), 7.5106 (19), 18.989 (4)	5.1576 (11), 7.307 (2), 18.888 (3)	5.2601 (13), 7.4275 (18), 19.062 (4)
Resolution (Å)‡		9.51–0.62 (0.63–0.62)	9.49–0.69 (0.70–0.69)	9.44–0.61 (0.62–0.61)	9.53–0.61 (0.62–0.61)
Completeness (%)‡		100.00 (100.00)	100.00 (100.00)	98.7 (96.4)	100.00 (100.00)
Multiplicity‡		29.5 (19.7)	30.3 (18.2)	18.1 (13.9)	29.5 (16.1)
I/σ‡		8.4 (0.5)	8.6 (0.7)	7.2 (0.5)	11.8 (1.0)
$CC_{1/2}$‡		0.995 (0.644)	0.995 (0.155)	0.992 (0.518)	0.994 (0.878)
Total reflections‡		56107 (1614)	43604 (1310)	34236 (1128)	59914 (1693)
Unique reflections‡		1905 (82)	1439 (72)	1892 (81)	2031 (105)
Kinematical refinement with neutral-atom model, with iSFAC charged-atom model					
R_1		0.197, 0.149	0.197, 0.161	0.174, 0.127	0.193, 0.136
wR_2		0.360, 0.299	0.374, 0.327	0.326, 0.259	0.369, 0.300
CCDC ID		–	–	2535386, 2535387	–
Dynamical refinement with neutral-atom model§					
R_1		–	–	0.153	–
wR_2		–	–	0.340	–
Z-score		–	–	4.279	–

† The value ranges and the standard deviations over multiple datasets are represented. ‡ Values in parentheses are for the highest resolution shell. § Values from refinement with L configuration using *JANA* for one of the collected datasets are represented.

integration of diffraction patterns, with corrections for elliptical distortion. Because JUNGFRAU tolerates direct-beam incidence, *JFGui* performs a parallel, real-time 2D Gaussian fit within a region of interest (ROI) around the direct beam, using only non-saturated pixels, to extract the amplitude, centroid (x_0, y_0), widths (σ_x, σ_y) and tilt θ, which are continuously displayed to guide focus adjustment (Ferjaoui *et al.*, 2025). In calibration mode, both the 1D intensity profile and the calculated camera length are displayed to verify ring positions against expected values. All calibration data and microscope parameters are stored in a JSON file, referenced throughout subsequent sessions. Fig. 2(*a*) represents this functionality and Movie 1 in the supporting information demonstrates a typical calibration measurement workflow.

2.2.4. Diffraction data collection and post-processing

Crystals for diffraction measurements are first identified in LowMAG mode (typically ×1200 magnification) and centered manually or by directly clicking the position within *JFGui*. The stage height is adjusted to maintain eucentricity, first coarsely in LowMAG and then precisely in MAG mode. After switching to DIFF mode, data collection proceeds with synchronized control of continuous stage rotation. Buffered frames are stored in a NeXus-compliant HDF5 file by *jfjoch_writer*, and *metadata-updater* appends microscope parameters (accelerating voltage, lens currents, aperture size and position, and stage coordinates), following the EMD format of electron microscopy (Savitzky, 2023) [Fig. 1(*b*)]. To secure the experimental data as self-contained for downstream analysis, each dataset stores the direct beam position, estimated dose, calibrated camera length, rotation axis and stage tilt-angle readout list during continuous rotation. The spot-plotter module provides a live 3D visualization of detected diffraction spots. Post-processing via *PostprocessServer_JFED* includes background subtraction, 3D spot finding and indexing with *XDS* (Kabsch, 2010*b*) supported by the Dectris *Neggia* plugin

Table 2
Measurement parameters and data collection statisticsfor PTCDI-C8 and perylene.

		PTCDI-C8	Perylene	
Molecular formula		$C_{20}H_{21}N_2O_4$	$C_{20}H_{12}$	$C_{20}H_{12}$
Sample temperature (K)		295	295	295
Detector		JUNGFRAU 1M	JUNGFRAU 1M	JUNGFRAU 1M
Frame rate (Hz)		2000	2000	2000
Frames summed		100	100	100
Data collection				
Electron microscope		JEOL JEM2100Plus	JEOL JEM2100Plus	JEOL JEM2100Plus
Accelerating voltage (kV)		200	100	200
Electron count rate ($Å^{-2}\,s^{-1}$)		0.10	0.10	0.10
Duration per single data collection (s)†		58.5–70.2	56.9–67.3	41.7–70.8
Rotation angle range (°)†		117.6–140.8	113.3–131.5	82.2–141.6
Stage rotation speed ($^\circ\,s^{-1}$)	Nominal	2.0	2.0	2.0
	Measured†	2.017 (4)	2.015 (4)	2.018 (5)
Camera length (mm)	Nominal	600	300	500
	Calibrated	912	510	764
Crystallographic data				
Processing software		*XDS*	*DIALS*	*DIALS*
Merging software		*xia2*	*xia2*	*xia2*
Number of crystal merged		9	3	4
Space group		$P\bar{1}$	$P2_1/c$	$P2_1/c$
a, b, c (Å)		4.8742 (4), 8.6387 (7), 20.782 (2)	10.328 (7), 10.795 (2), 11.377 (4)	10.310 (5), 10.868 (2), 11.360 (4)
α, β, γ (°)		83.498 (7), 89.543 (7), 81.595 (6)	90, 100.71 (4), 90	90, 100.50 (4), 90
Resolution (Å)‡		20.65–1.00 (1.02–1.00)	7.86–0.90 (0.92–0.90)	11.14–0.74 (0.75–0.74)
Completeness (%)‡		97.3 (96.6)	89.1 (89.5)	92.3 (90.9)
Multiplicity‡		10.1 (11.2)	8.4 (9.0)	8.6 (8.7)
I/σ‡		29.6 (11.6)	4.7 (0.4)	4.1 (0.3)
$CC_{1/2}$‡		0.969 (0.642)	0.982 (0.521)	0.996 (0.378)
Total reflections†		17659 (967)	14687 (767)	29236 (1462)
Unique reflections‡		1748 (86)	1757 (85)	3385 (169)
Kinematical refinement with neutral-atom model, with iSFAC charged-atom model				
R_1		0.245, 0.239	0.197, –§	0.199, 0.176
wR_2		0.498, 0.485	0.399, –§	0.401, 0.374
CCDC ID		2535388, 2535389	–	–

† The value ranges and the standard deviations over multiple datasets are represented. ‡ Values in parentheses are for the highest resolution shell. § Refinement with iSFAC model did not converge.

(Dectris, 2017), and optionally with *DIALS* (Winter *et al.*, 2018). Upon successful indexing, lattice parameters and crystal orientations are displayed in *JFGui*. The orientation matrices visualize the variation across collected datasets on the 2D grid atlas and 3D spot plotter. Subsequent processing steps—refinement, integration, scaling, merging and phasing—are supported through *XSCALE* and *XDSCONV* (Kabsch, 2010*a*), *DIALS*, *xia2* (Winter, 2010) and *SHELXT* (Sheldrick, 2015*b*). When phasing succeeds, *ShelXle* (Hübschle *et al.*, 2011; Sheldrick, 2015*a*) launches automatically to display the initial structure model. Crystallographic statistics and experimental metadata are summarized in a JSON file and visualized within *JFGui*. The *CCDCscreener* compares the determined lattice with CCDC entries and lists potential matches. Figs. 2(*b*) and 2(*c*) summarize the workflow and provide representative display outputs, and Movies 2 and 3 show a practical case described in Sections 3.2.1 and 3.2.3.

3. Results and discussion

Tables 1 and 2 list all experimental parameters and crystallographic statistics of this section. Atomic charges determined with the iSFAC charged-atom model are provided in Tables S1–S3.

3.1. Static beam stability and reproducibility on mode-switching

The radiation hardness of the JUNGFRAU allows us to record the direct beam and quantify its stability under typical 3D ED conditions. For each frame, the direct-beam spot is fitted with a rotated 2D super-Gaussian, and the beam intensity is defined as the integrated counts inside a 2σ ellipse around the fitted centroid [Fig. 3(*a*)]. The beam position remains stable within one pixel over a typical 3D ED data-collection time (∼3 min). The corresponding frame-to-frame fluctuations of the direct-beam intensity are limited to ∼2–3% relative standard deviation. Compared with the variation in effective crystal thickness during continuous rotation—often exceeding 100% over a tilt range of ∼60°—such intensity fluctuations are minor and can be sufficiently compensated for by scaling procedures in subsequent data-processing stages.

In the proposed workflow, the TEM magnification mode is switched frequently. Although this flexibility allows users to

efficiently search for crystals and perform diffraction measurements, hysteresis effects in the electromagnetic lenses may induce unintended focus shifts, potentially requiring refocusing after each mode change. To evaluate focus reproducibility under such conditions, Fig. 4 presents an assessment using an aluminium standard grid. A series of image frames was recorded while repeatedly switching between DIFF, MAG and LowMAG modes. For frames acquired in DIFF mode, beam centering and focus quality were quantified using the direct-beam position and the intensities of major peaks in the aluminium Debye–Scherrer rings, respectively. Although the beam position exhibited shifts upon mode switching, the diffraction peak intensities remained largely consistent within the level of statistical fluctuation. This indicates that lens hysteresis is reproducible across the three magnification modes, and that a focusing operation to calibrate the focal plane is required only at the initial setup. Since the beam position is determined for each dataset in processing using the *EPOC* software suite (*JFGui* and *PostprocessServer_JFED*; see the following section), these positional shifts do not adversely affect subsequent data processing.

3.2. Crystallographic applications

3.2.1. Standard and applied use cases

Fig. 5 presents the structures and the atomic charges determined through the proposed workflow. Histidine serves as a benchmark compound in 3D ED. Using the conventional neutral-atom model, residual negative features are observed between atoms in the difference electrostatic potential map, indicating valence electrons. Applying the iSFAC charged-atom model via *ShelXFile_EDiSFAC*, these residual features disappear [Figs. 5(*a*) and 5(*b*)], confirming the improved modeling of charge redistribution. Despite retaining spherical atomic scattering factors, iSFAC introduces one charge-transfer term per atom (Mahmoudi *et al.*, 2025), yielding

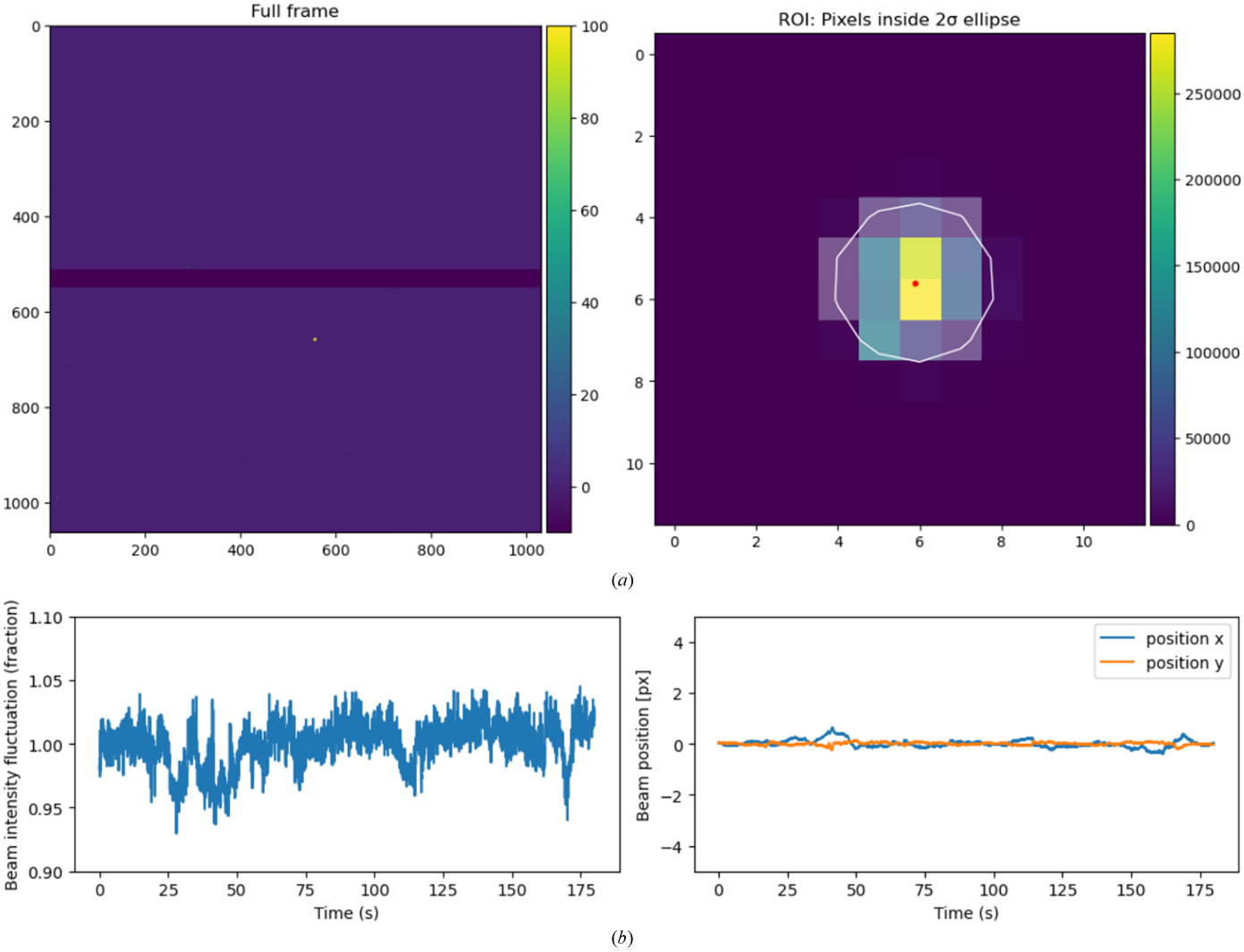


Figure 3
Static beam stability evaluated using the JUNGFRAU detector. (*a*) Definition of direct-beam properties using a 2D super-Gaussian fit (Ferjaoui *et al.*, 2025). Beam intensity is quantified by integrating counts within the fitted elliptical region (right panel). (*b*) Temporal evolution of direct-beam intensity (left) and beam position (right) during continuous frame acquisition. To avoid pixel overload, data acquisition was performed at a reduced count rate corresponding to 1% of the standard configuration.

refined charges of +0.54 (5) for the amino group and −0.62 (5) for the carboxylate moiety. Because histidine is a chiral molecule and crystallized in a non-centrosymmetric space group ($P2_12_12_1$), the absolute configuration is chemically relevant. Using the *DIALS* output, dynamical refinement with *JANA* (Petříček *et al.*, 2023) successfully established the L configuration, supported by the *Z*-score (Table 1) (Klar *et al.*, 2023; Vypritskaia *et al.*, 2025). This dynamical refinement step is not yet integrated into our standard workflow and currently requires manual processing. As in the previous study, data from multiple crystals were merged to reduce crystal-dependent variation; nevertheless, residual systematic effects

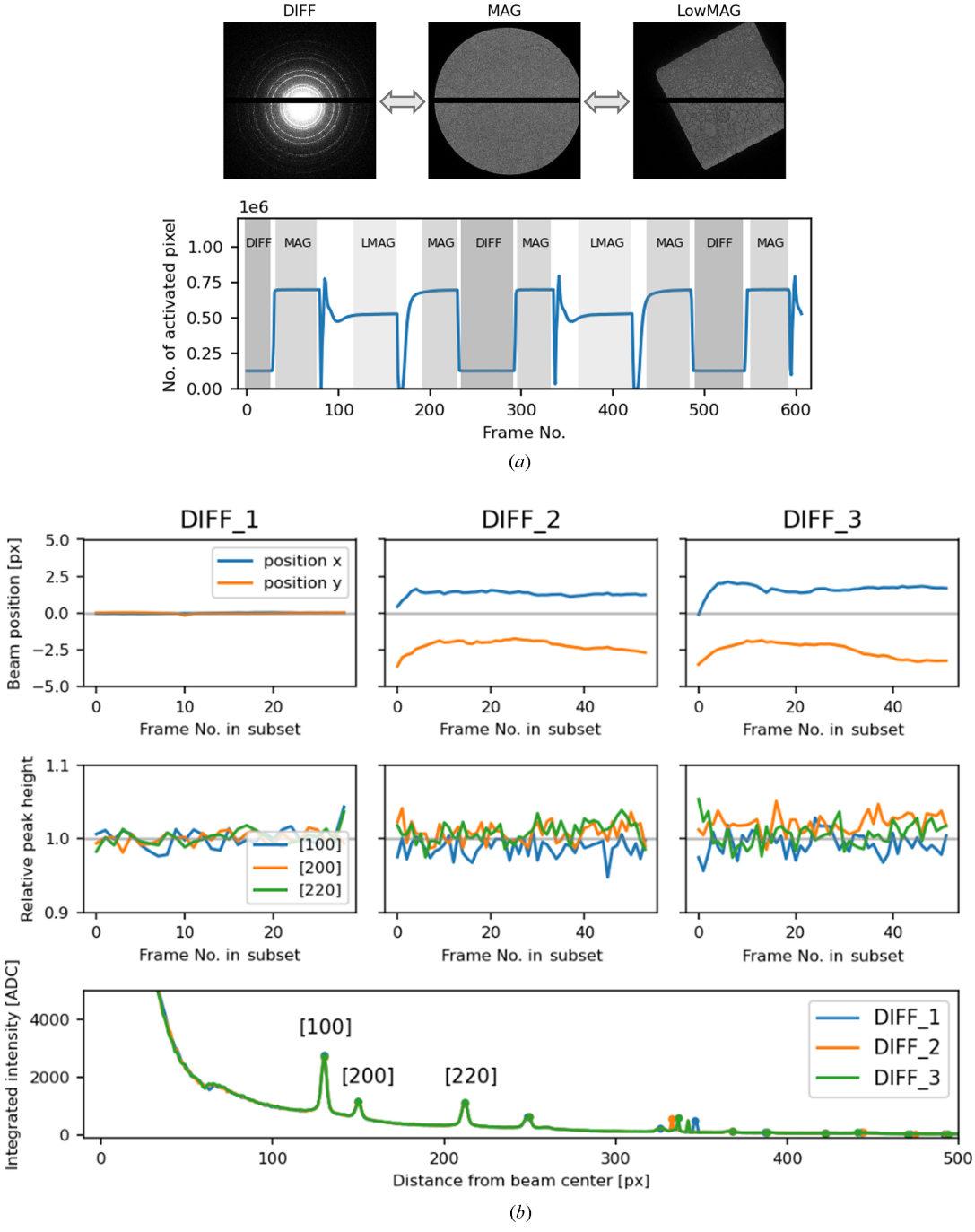


Figure 4
Beam focus reproducibility during magnification-mode switching. (*a*) (Top) Representative images acquired in DIFF, MAG and LowMAG modes, which are typically used for diffraction measurements, fine crystal alignment and crystal searching, respectively. (Bottom) Number of pixels detecting more than two electrons per frame in a continuous TEM image series, during which TEM modes were switched intermittently. As the illumination area depends on the TEM mode, the active mode can be identified on a per-frame basis, excluding intermediate transition frames. (*b*) Temporal evolution of the direct-beam position (top) and diffraction peak intensity (middle) for three frame subsets acquired in DIFF mode. The three major peaks in the azimuth integration profile (100, 200 and 220; bottom) are shown for comparison. These profiles mostly overlap, indicating stable focus reproduction despite multiple lens-current changes during mode switching.

from dynamical scattering cannot be quantified with the present procedure.

As a second sample, PTCDI-C8 is an organic semiconductor with a known triclinic structure determined previously by single-crystal X-ray diffraction (SXRD) at −143°C (Briseno *et al.*, 2007). The workflow reproduced the same structure from nanowire crystals at room temperature, which are otherwise challenging for direct analysis. The determined atomic charges for the alkyl terminals and the π-conjugated core are +0.7 (2) and −0.7 (2), respectively, suggesting electron redistribution between these moieties [Figs. 5(*c*) and 5(*d*)]. This illustrates that the workflow can support both standard and advanced applications of 3D ED.

3.2.2. Data collection with high-speed rotation

The JUNGFRAU detector supports data acquisition at 2 kHz, and in standard operation, images are summed over 20 frames for display and recording, corresponding to rotation slices of 0.025–0.10° at stage speeds of 0.5–2.0° s^{-1}. This provides adequate sampling for typical organic crystals while extending dynamic range and reducing storage and graphic computation demands. To test the limits of the workflow, continuous-rotation datasets were collected at the JEM2100Plus stage's maximum nominal speed of 10° s^{-1}. Fig. 6(*a*) compares nominal and readout values of rotation angles in single datasets collected at two different speeds. Approximately 10% deviation was observed at 10° s^{-1}, in contrast to ∼1% at 2.0° s^{-1}. This difference was reproducible across rotation, but the variance was not negligible [Fig. 6(*b*)]. In the post-processing pipeline (Section 2.2.4), the average of the readout values is used for each rotation, with outliers and systematic errors excluded.

Figs. 6(*c*) and 6(*d*) show data statistics and refined bond lengths for L-histidine collected at 2.0 and 10° s^{-1} nominal rotation speed, under both room-temperature (RT) and

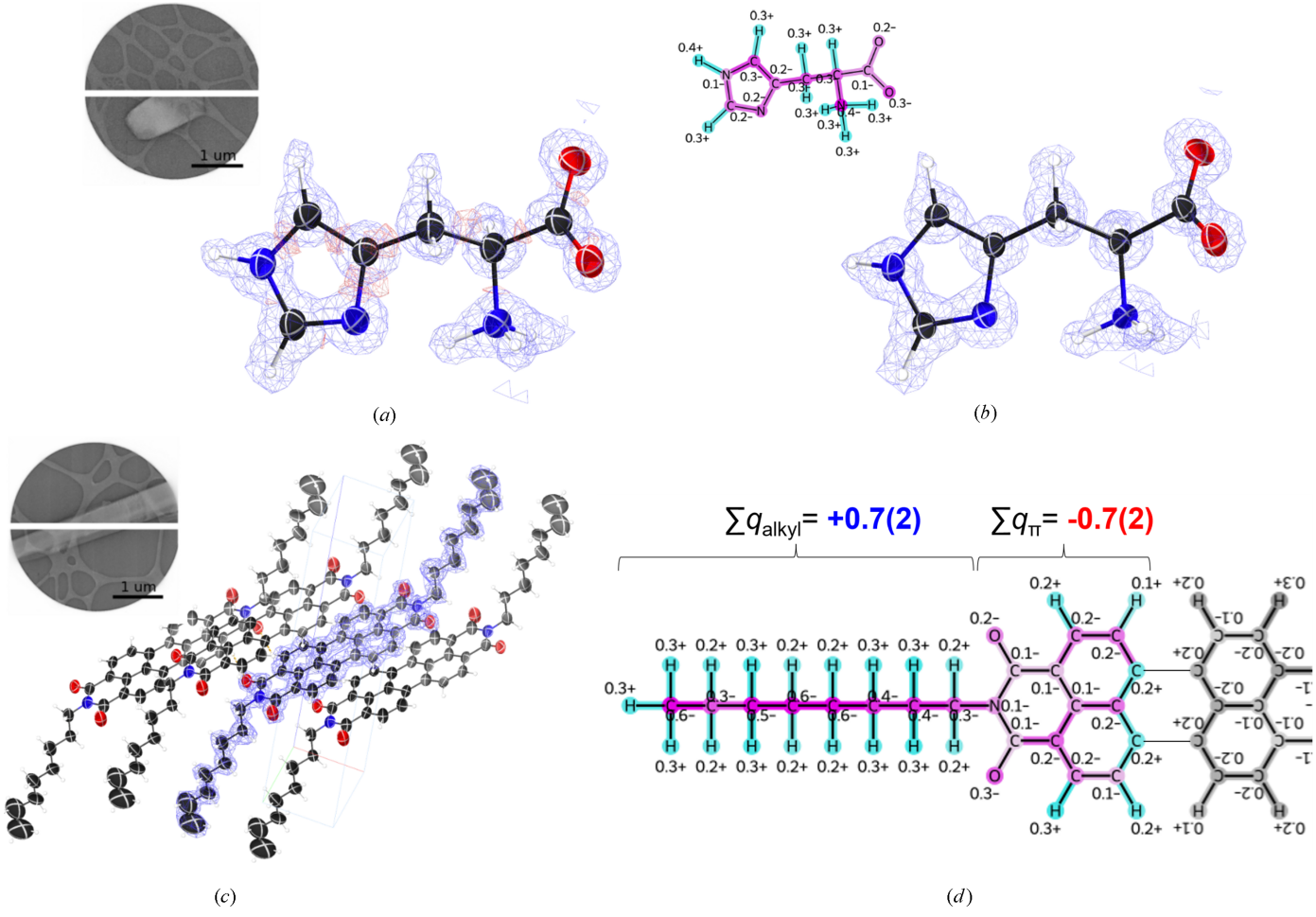


Figure 5
Structures resolved by the 3D ED workflow with JUNGFRAU. (*a*) Structure and electrostatic potential maps of L-histidine refined using conventional neutral-atom modeling. (*b*) Structure and maps after applying the iSFAC charged-atom model. The F_{obs} maps are shown in blue (0.32 e^{-} Å^{-1}), and the $F_{obs} - F_{calc}$ maps (−0.17 e^{-} Å^{-1}) are shown in red. In both cases, no continuous positive residual volume remains; in (*b*), negative residual volume is also absent. The inset in (*b*) shows the determined atomic charges. (*c*) Crystal structure of PTCDI-C8. The F_{obs} map (0.12 e^{-} Å^{-1}) is overlaid on the model at the center. (*d*) Determined atomic charges for PTCDI-C8. Half of the molecule is modeled on the basis of inversion symmetry. Partial sums of the alkyl and π-conjugated regions are indicated. The estimated standard deviations are displayed in parentheses. Insets in (*a*) and (*c*) show typical crystal images. 3D and 2D molecular pictures in (*a*–*c*) and (*b*, *d*) were created using *ShelXle* (Hübschle *et al.*, 2011) and *RDkit* (Landrum, 2016), respectively.

cryogenic (−110°C) conditions. The beam illumination was adjusted to ∼1.3 e^{-} Å^{-2} per crystal for either case. For RT data, high-speed acquisition produced slightly inferior statistics and one outlier bond length in the carboxylate group, probably due to crystal motion induced by higher instantaneous dose (Vlahakis *et al.*, 2025; Vinothkumar & Henderson, 2016; Scheres, 2014). Cryogenic measurements suppressed this effect, yielding stable geometries even at 10° s^{-1}. These results demonstrate that high-speed continuous rotation is feasible within the workflow, provided that the reduced dynamic range and increased per-second dose are considered.

A full ∼130° rotation can be acquired in ∼15 s, enabling rapid dataset collection which creates additional scope for obtaining more datasets and performing intermediate processing. Since the initial stage of the post-processing is sufficiently fast, indexing results are displayed before subsequent data collection starts. The time required for complete structure determination still depends on the performance of the downstream crystallographic programs.

3.2.3. Verification of beam-energy contribution

The JUNGFRAU detector and the workflow support data collection at various beam energies. In the previous study, we evaluated the spatial resolution of the JUNGFRAU over an electron energy range from 70 to 200 keV (Ferjaoui *et al.*, 2025). There, higher spatial resolution was demonstrated at lower beam energies, owing to the reduced multiple scattering and lateral diffusion. The concept of exploiting lower-energy beams has also been proposed in imaging studies (Peet *et al.*, 2019; Naydenova *et al.*, 2019; McMullan *et al.*, 2023).

In Fig. 7, measurements with 100 and 200 kV beams are compared for perylene crystals, which are relatively radiation resistant due to the π-conjugated structure. Under illumination of the same electron count on the same crystal [Figs. 7(*a*) and 7(*b*)], the real-space image under the 100 kV beam exhibited higher contrast than that with the 200 kV beam, as highlighted in the power spectra. On the other hand, the diffraction image recorded at 200 kV exhibited substantially higher quality. This difference becomes more evident for collected 3D ED datasets. Despite comparable counts of electrons being exposed (∼6.5 e^{-} Å^{-2} per crystal), the I/σ and $CC_{1/2}$ statistics [Fig. 7(*c*)] were consistently superior for the 200 kV dataset, and the refined bond lengths agreed more closely with the SXRD reference structure (Näther *et al.*, 1998). The two bridging C—C bonds between naphthalene units (C8—C18 and C10—C20) were distinguishable as single bonds at 200 kV, but not at 100 kV [Fig. 7(*d*)].

This behavior is primarily attributable to crystal thickness. The penetration depth of 100 kV electrons in graphite is 71 µm, in contrast to 233 µm at 200 kV (ICRU, 2014). Estimates that account for elastic and inelastic scattering contribution indicate that only crystals thinner than ∼65 nm (or ∼33 nm when tilted ±60°) benefit from lower voltages

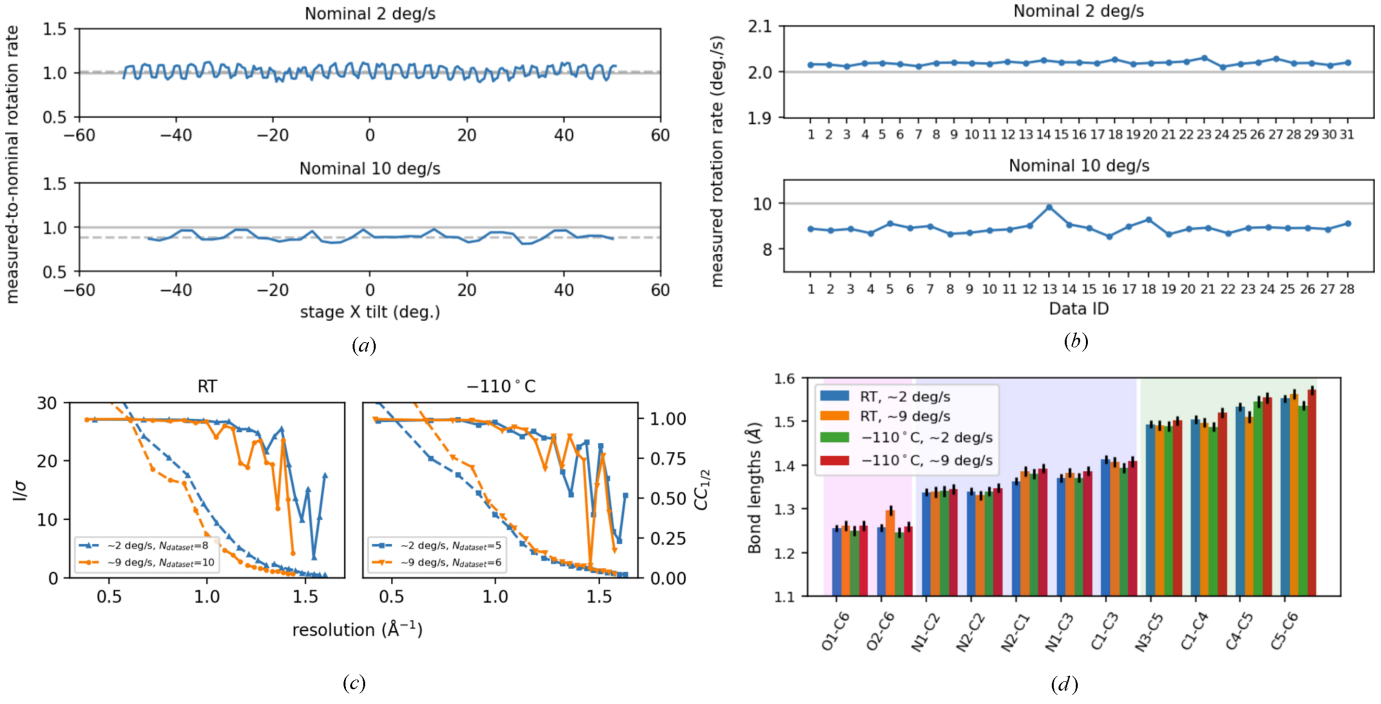


Figure 6
Verification of high-speed continuous-rotation data collection. (*a*) Ratios of readout to nominal tilt angles during single rotation at nominal speeds of 2° s^{-1} (top) and 10° s^{-1} (bottom). The solid gray line represents the nominal value and the dashed line represents the mean value over the rotation. (*b*) Mean readout value for multiple independent rotations at 2° s^{-1} (top) and at 10° s^{-1} (bottom). The solid gray line represents the nominal value. (*c*) Statistics per resolution shell for L-histidine data collected at RT (left) and cryogenic (−110°C, right) conditions. The solid lines are $CC_{1/2}$ on the right axes, and the dashed lines are for I/σ on the left axes. (*d*) The determined bond lengths of L-histidine. The error bars indicate the estimated standard deviations. Background shading indicates bond types (carboxylic, aromatic and single).

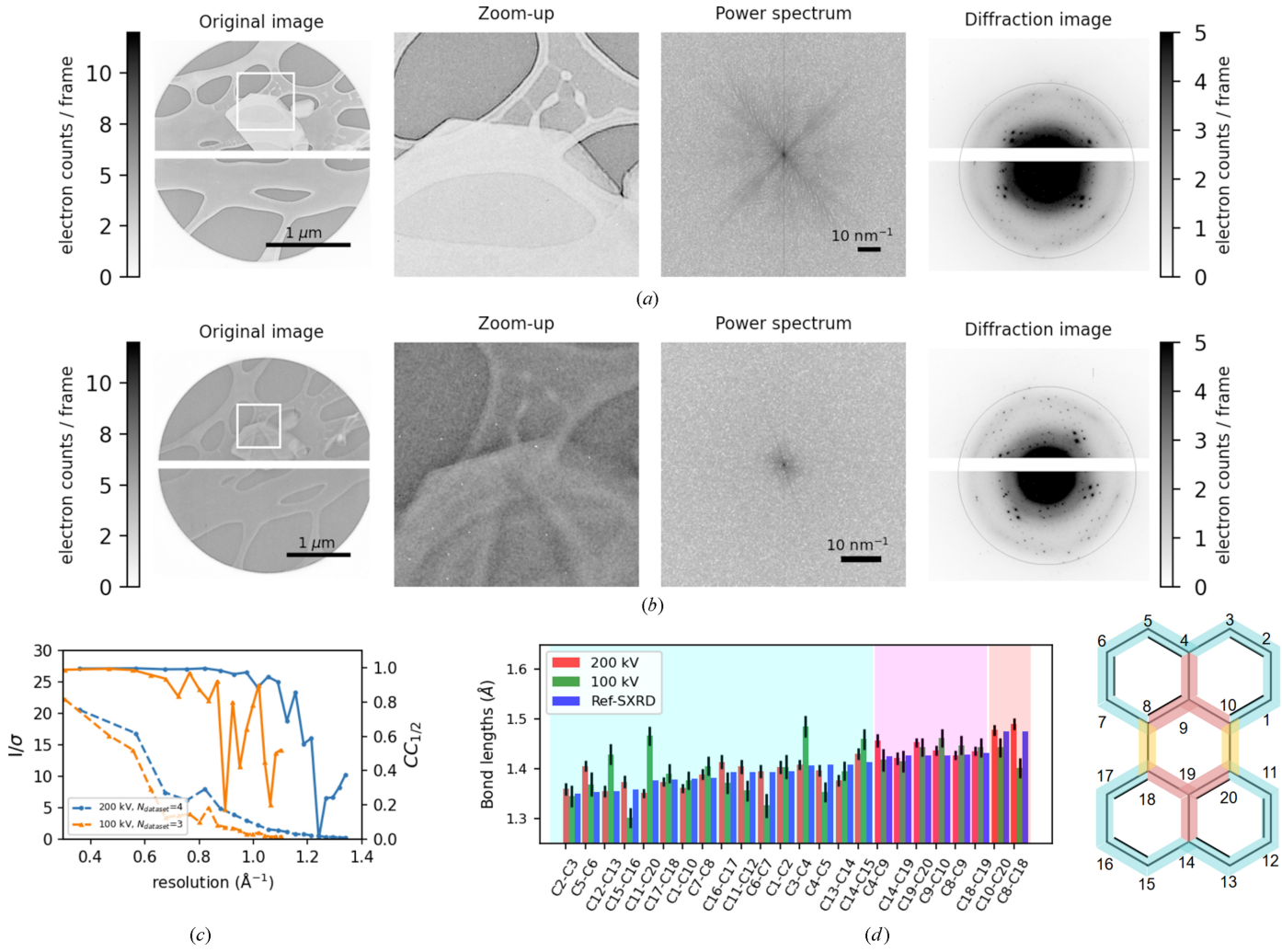


Figure 7
Real- and reciprocal-space resolution of perylene crystals measured with 100 and 200 kV electron beams. (*a*, *b*) Real-space (left) and diffraction (right) images of the same crystal acquired at 100 kV (*a*) and 200 kV (*b*). The two middle panels show a magnified view of a selected region in the real-space image and its corresponding power spectrum. The contrast scales are indicated by the bars on each side. The gray ring in the diffraction image indicates a resolution of 1 Å. (*c*) Dataset statistics per resolution shell. The solid lines are for $CC_{1/2}$ on the right axes, and the dashed lines are for I/σ on the left axes. (*d*) The determined bond lengths. The error bars indicate the estimated standard deviation. For reference, the SXRD structure measured under room temperature from CCDC depositions is shown (Näther *et al.*, 1998). Atomic labels correspond to the chemical formula in the right panel, and bonds are colored according to their environment.

(Peet *et al.*, 2019). This requirement is stringent for diffraction measurement with the perylene crystals conducted here, and in practice, the higher-quality structure was obtained with the 200 kV beam, regardless of improved detector resolution. In general, the optimal accelerating voltage depends on both samples and microscopes. Factors such as the energy deposited by electrons in the sample, beam divergence and stability at different energies can also influence the quality of diffraction data.

4. Conclusions and outlook

In this work, we established an integrated hardware–software platform for 3D ED employing the JUNGFRAU 1M detector. The workflow combines the FPGA-based Jungfraujoch backend with the *JFGui* interface to coordinate the detector, microscope and processing modules in a unified environment. This integration enables fully synchronized data acquisition, metadata management and post-processing within a single, user-accessible framework. Application to L-histidine and PTCDI-C8 crystals demonstrated that structures can be resolved with charge-density evaluation using the iSFAC method, highlighting the system's capability for sub-atomic structural chemistry. Further assessments on broader classes of materials will extend the feasibility of this approach.

Beyond standard applications, the system performance was examined with respect to calibration accuracy, data-collection speed and beam-energy dependence. Continuous-rotation data collection at up to $10^{\circ}\ s^{-1}$ was achieved without loss of data integrity, demonstrating the feasibility of high-throughput acquisition. The platform's compatibility with 100 and 200 keV beam energies revealed the practical trade-off

between real-space contrast and reciprocal-space resolution, suggesting that lower-energy beams are expected to be adventageous for sufficiently thin specimens.

These developments represent important steps toward making 3D ED more practical and accessible through the use of the JUNGFRAU detector. By integrating high-speed data acquisition, adaptive calibration and live analysis into a cohesive workflow, the proposed platform shortens the experimental feedback cycle and reduces the practical effort required for routine 3D ED experiments. In particular, the integrated post-processing pipeline, together with immediate presentation of the processing results, allows users to evaluate data quality during acquisition and adapt the measurement strategy before collecting subsequent datasets, thereby improving the efficiency of data collection. This integrated workflow enables crystallographers to explore advanced methodology while also providing perspectives toward future instrument development.

This work in addition demonstrates a development model for emerging analytical techniques. Detector technologies have largely been advanced within large-scale facilities, particularly synchrotron and XFEL environments, where extensive resources are available. In contrast, the present platform was developed and validated within an in-house laboratory environment, illustrating how modern detector technologies can be translated into practical research tools outside major facilities. Such efforts are increasingly important for broadening access to advanced instrumentation and accelerating methodological dissemination.

Acknowledgements

TG and EF initiated the project and acquired the funding. KF, EF and TG set up the hardware environment. KT, KF, EF and TG developed the software and KT and TG tested it for debugging. KT, KF, EF and TG contributed on the experimental design. KT prepared the sample crystals and conducted data collection, processing and analysis. KT wrote the initial draft. Large language models were used in order to paraphrase and improve readability. All authors gave their input on it and consented to the submission of the final version. The authors thank Dr Steven van Terwingen for reading and discussing the manuscript and for testing the GUI, and Katarína Šťastná and Dr Soheil Mahmoudi for testing the GUI. The authors thank Dr Filip Leonarski for help to stabilize the Junfraujoch backend on our setup. This research was funded in part by the Austrian Science Fund (FWF) (I6546-N; 'Electrostatic potential through charge-integration'; https://doi.org/10.55776/I6546). Open access publishing facilitated by ETH-Bereich Forschungsanstalten, as part of the Wiley–ETH-Bereich Forschungsanstalten agreement via the Consortium of Swiss Academic Libraries.

Conflict of interest

The authors declare that the research was conducted in the absence of any commercial or financial relationships that could be construed as a potential conflict of interest.

Data availability

The source code is freely available on GitHub (https://github.com/epoc-ed) and the package used in this study has been archived on Zenodo (https://doi.org/10.5281/zenodo.20867896). Crystal structures of the compounds studied here are available as `.cif` files. The neutral- and iSFAC charged-atom models of L-histidine at −110°C and PTCDI-C8 at RT have been deposited with the CCDC (deposition Nos. 2535386, 2535387, 2535388 and 2535389). An example diffraction dataset from this work is available at https://zenodo.org/records/18606359 (L-histidine). Other raw data, program code and analysis scripts are available upon request from the authors.

Funding information

This research was funded in part by the Austrian Science Fund (FWF) (grant 10.55776/I6546) and by the Swiss National Science Foundation (grant 215650).

References

Briseno, A. L., Mannsfeld, S. C. B., Reese, C., Hancock, J. M., Xiong, Y., Jenekhe, S. A., Bao, Z. & Xia, Y. (2007). *Nano Lett.* **7**, 2847–2853.

Dectris (2017). *Neggia*, https://github.com/dectris/neggia.

de la Cruz, M. J., Martynowycz, M. W., Hattne, J. & Gonen, T. (2019). *Ultramicroscopy* **201**, 77–80.

Egerton, R. (2019). *Micron* **119**, 72–87.

Ferjaoui, K., Takaba, K., Gruene, T., Fröjdh, E., Bergamaschi, A., Brückner, M., Carulla, M., Dinapoli, R., Ebner, S., Gautam, V., Greiffenberg, D., Hasanaj, S., Heymes, J., Hinger, V., Hürst, M., Kedych, V., King, T., Li, S., Leonarski, F., Lopez-Cuenca, C., Mazzoleni, A., Mezza, D., Moustakas, K., Mozzanica, A., Mulvey, J., Müller, M., Paton, K. A., Posada Soto, C., Ruder, C., Schmitt, B., Sieberer, P., Silletta, S., Thattil, D., Xie, X. & Zhang, J. (2025). *J. Instrum.* **20**, C12007–C12007.

Fröjdh, E., Bergamaschi, A. & Schmitt, B. (2024). *Front. Phys.* **12**, 1304896.

Fröjdh, E., Wennmacher, J., Rzepka, P., Mozzanica, A., Redford, S., Schmitt, B., van Bokhoven, J. & Gruene, T. (2020). *Crystals* **10**, 1148.

Gemmi, M., Mugnaioli, E., Gorelik, T. E., Kolb, U., Palatinus, L., Boullay, P., Hovmöller, S. & Abrahams, J. P. (2019). *ACS Cent. Sci.* **5**, 1315–1329.

Groom, C. R., Bruno, I. J., Lightfoot, M. P. & Ward, S. C. (2016). *Acta Cryst.* B**72**, 171–179.

Gruene, T., Wennmacher, J. T. C., Zaubitzer, C., Holstein, J. J., Heidler, J., Fecteau–Lefebvre, A., De Carlo, S., Müller, E., Goldie, K. N., Regeni, I., Li, T., Santiso–Quinones, G., Steinfeld, G., Handschin, S., van Genderen, E., van Bokhoven, J. A., Clever, G. H. & Pantelic, R. (2018). *Angew. Chem. Int. Ed.* **57**, 16313–16317.

Howells, M., Beetz, T., Chapman, H., Cui, C., Holton, J., Jacobsen, C., Kirz, J., Lima, E., Marchesini, S., Miao, H., Sayre, D., Shapiro, D., Spence, J. & Starodub, D. (2009). *J. Electron Spectrosc. Relat. Phenom.* **170**, 4–12.

Hübschle, C. B., Sheldrick, G. M. & Dittrich, B. (2011). *J. Appl. Cryst.* **44**, 1281–1284.

ICRU (2014). ICRU Report 14, pp. 1–110. International Commission on Radiation Units and Measurements, Washington, DC, USA.

Ito, S., White, F. J., Okunishi, E., Aoyama, Y., Yamano, A., Sato, H., Ferrara, J. D., Jasnowski, M. & Meyer, M. (2021). *CrystEngComm* **23**, 8622–8630.

JEOL (2018). *PyJEM: External Control of JEOL TEM*, https://github.com/PyJEM/PyJEM.
Kabsch, W. (2010*a*). *Acta Cryst.* D**66**, 133–144.
Kabsch, W. (2010*b*). *Acta Cryst.* D**66**, 125–132.
Klar, P. B., Krysiak, Y., Xu, H., Steciuk, G., Cho, J., Zou, X. & Palatinus, L. (2023). *Nat. Chem.* **15**, 848–855.
Kratzert, D. (2018). *Shelxfile*, https://github.com/dkratzert/ShelXFile.
Landrum, G. (2016). *RDKit: Open-Source Cheminformatics Software*, https://www.rdkit.org.
Leonarski, F., Brückner, M., Lopez-Cuenca, C., Mozzanica, A., Stadler, H.-C., Materěj, Z., Castellane, A., Mesnet, B., Wojdyla, J. A., Schmitt, B. & Wang, M. (2023). *J. Synchrotron Rad.* **30**, 227–234.
Leonarski, F., Redford, S., Mozzanica, A., Lopez-Cuenca, C., Panepucci, E., Nass, K., Ozerov, D., Vera, L., Olieric, V., Buntschu, D., Schneider, R., Tinti, G., Froejdh, E., Diederichs, K., Bunk, O., Schmitt, B. & Wang, M. (2018). *Nat. Methods* **15**, 799–804.
Li, T., Melis, S., Bagade, C., Khatib, A., Kosarzycki, R., Maglieri, G., Zhang, X. & Van Keuren, E. (2019). *J. Nanopart. Res.* **21**, 147.
Mahmoudi, S., Gruene, T., Schröder, C., Ferjaoui, K. D., Fröjdh, E., Mozzanica, A., Takaba, K., Volkov, A., Maisriml, J., Paunović, V., van Bokhoven, J. A. & Keppler, B. K. (2025). *Nature* **645**, 88–94.
Maisriml, J. & Gruene, T. (2024). *Singla GUI – A Graphical User Interface for the SINGLA Detector and TEM*, https://github.com/tgruene/SinglaGUI.
Martynowycz, M. W., Clabbers, M. T. B., Hattne, J. & Gonen, T. (2022). *Nat. Methods* **19**, 724–729.
Mastronarde, D. N. (2005). *J. Struct. Biol.* **152**, 36–51.
McMullan, G., Naydenova, K., Mihaylov, D., Yamashita, K., Peet, M. J., Wilson, H., Dickerson, J. L., Chen, S., Cannone, G., Lee, Y., Hutchings, K. A., Gittins, O., Sobhy, M. A., Wells, T., El-Gomati, M. M., Dalby, J., Meffert, M., Schulze-Briese, C., Henderson, R. & Russo, C. J. (2023). *Proc. Natl Acad. Sci. USA* **120**, e2312905120.
Mozzanica, A., Bergamaschi, A., Brueckner, M., Cartier, S., Dinapoli, R., Greiffenberg, D., Jungmann-Smith, J., Maliakal, D., Mezza, D., Ramilli, M., Ruder, C., Schaedler, L., Schmitt, B., Shi, X. & Tinti, G. (2016). *J. Instrum.* **11**, C02047.
Näther, C., Bock, H., Havlas, Z. & Hauck, T. (1998). *Organometallics* **17**, 4707–4715.
Naydenova, K., McMullan, G., Peet, M. J., Lee, Y., Edwards, P. C., Chen, S., Leahy, E., Scotcher, S., Henderson, R. & Russo, C. J. (2019). *IUCrJ* **6**, 1086–1098.
Pacoste, L., Ignat'ev, V. M., Dominiak, P. M. & Zou, X. (2024). *IUCrJ* **11**, 878–890.
Parkhurst, J. M., Crawshaw, A. D., Siebert, C. A., Dumoux, M., Owen, C. D., Nunes, P., Waterman, D., Glen, T., Stuart, D. I., Naismith, J. H. & Evans, G. (2023). *IUCrJ* **10**, 270–287.
Peet, M. J., Henderson, R. & Russo, C. J. (2019). *Ultramicroscopy* **203**, 125–131.
Petříček, V., Palatinus, L., Plášil, J. & Dušek, M. (2023). *Z. Kristallogr.* **238**, 271–282.
Roslova, M., Smeets, S., Wang, B., Thersleff, T., Xu, H. & Zou, X. (2020). *J. Appl. Cryst.* **53**, 1217–1224.
Sasaki, T., Nakane, T., Kawamoto, A., Nishizawa, T. & Kurisu, G. (2023). *CrystEngComm* **25**, 352–356.
Savitzky, B. (2023). *emdfile*, https://github.com/py4dstem/emdfile.
Scheres, S. H. (2014). *eLife* **3**, e03665.
Sheldrick, G. M. (2015*a*). *Acta Cryst.* C**71**, 3–8.
Sheldrick, G. M. (2015*b*). *Acta Cryst.* A**71**, 3–8.
Smeets, S., Zou, X. & Wan, W. (2018). *J. Appl. Cryst.* **51**, 1262–1273.
Suresh, A., Yörük, E., Cabaj, M. K., Brázda, P., Výborný, K., Sedláček, O., Müller, C., Chintakindi, H., Eigner, V. & Palatinus, L. (2024). *Nat. Commun.* **15**, 9066.
Takaba, K., Maki-Yonekura, S., Inoue, I., Tono, K., Hamaguchi, T., Kawakami, K., Naitow, H., Ishikawa, T., Yabashi, M. & Yonekura, K. (2023). *Nat. Chem.* **15**, 491–497.
Takaba, K., Maki-Yonekura, S. & Yonekura, K. (2020). *J. Struct. Biol.* **211**, 107549.
Tinti, G., Fröjdh, E., van Genderen, E., Gruene, T., Schmitt, B., de Winter, D. A., Weckhuysen, B. M. & Abrahams, J. P. (2018). *IUCrJ* **5**, 190–199.
van Genderen, E., Clabbers, M. T. B., Das, P. P., Stewart, A., Nederlof, I., Barentsen, K. C., Portillo, Q., Pannu, N. S., Nicolopoulos, S., Gruene, T. & Abrahams, J. P. (2016). *Acta Cryst.* A**72**, 236–242.
Vinothkumar, K. R. & Henderson, R. (2016). *Q. Rev. Biophys.* **49**, e13.
Vlahakis, N., Clauss, A. & Rodriguez, J. A. (2025). *IUCrJ* **12**, 223–238.
Vypritskaia, A., Zou, X., Yang, T. & Waterman, D. G. (2025). *Acta Cryst.* C**81**, 1–13.
Wang, B., Zou, X. & Smeets, S. (2019). *IUCrJ* **6**, 854–867.
Winter, G. (2010). *J. Appl. Cryst.* **43**, 186–190.
Winter, G., Waterman, D. G., Parkhurst, J. M., Brewster, A. S., Gildea, R. J., Gerstel, M., Fuentes-Montero, L., Vollmar, M., Michels-Clark, T., Young, I. D., Sauter, N. K. & Evans, G. (2018). *Acta Cryst.* D**74**, 85–97.
Yonekura, K., Matsuoka, R., Yamashita, Y., Yamane, T., Ikeguchi, M., Kidera, A. & Maki-Yonekura, S. (2018). *IUCrJ* **5**, 348–353.
Yörük, E., Klein, H. & Kodjikian, S. (2024). *Ultramicroscopy* **255**, 113857.
Zuo, J. M., Kim, M., O'Keeffe, M. & Spence, J. C. (1999). *Nature* **401**, 49–52.